Computational study on turbulent flows around modern tanker hull forms

Wu-Joan Kim[*,†], Do-Hyun Kim and Suak-Ho Van

Korea Research Institute of Ships & Ocean Engineering, KORDI, Jang-dong 171, Yusong-gu,
Taejon 305-343, South Korea

SUMMARY

To enhance the applicability of CFD techniques to the hull form design of modern commercial ships, an efficient and robust numerical method for turbulent flow calculation is developed. The preprocessor is composed of hull form presentation, surface mesh generation, and field grid generation. The finite-volume method is utilised to solve the Reynolds-averaged Navier–Stokes equations. Three $k-\varepsilon$ turbulence models, i.e., the standard $k-\varepsilon$ model (SKE), the RNG-based $k-\varepsilon$ model (RNG), and the realisable $k-\varepsilon$ model (RKE), are evaluated to investigate the difference caused by the turbulence model. The developed numerical method is applied to two practical VLCC hull forms with the same forebody and the slightly different afterbodies in order to find out whether CFD can capture the difference of stern flow due to hull form variation. It is found that RKE successfully predict the strength and location of bilge vortex, while SKE and RNG fail. However, all three models can provide the right information on the nominal wake difference between two hull forms. Copyright © 2002 John Wiley & Sons, Ltd.

KEY WORDS: VLCC; stern flow; grid generation; turbulence model; propeller plane wake

1. INTRODUCTION

The performance prediction of a commercial ship is usually carried out in the towing tank. However, it takes several months and big cost. Thus, the hull form designer is apt to rely on his intuition and personal experience rather than solid physical evidence. As indicated by the ITTC resistance committee [1], it is very probable that the viscous flow calculation methods will be used in the near future for the hull form evaluation even in commercial shipyards. The CFD technique will provide an opportunity to link the performance of the ship directly to flow phenomena around it. For the practical application of viscous flow calculation methods to evaluating hull forms, computational efforts should be affordable within the routine design process of a ship. It also should be confirmed that CFD can tell the flow difference due to hull form modification.

---

[*]Correspondence to: W.-J. Kim, Korea Research Institute of Ships & Ocean Engineering, Jang-dong 171, Yusong-gu, Taejon 305-343, South Korea.
[†]E-mail: wjkim@kriso.re.kr

There have been several workshops on viscous flow around a ship (e.g., 1990 SSPA-CTH-IIHR Workshop [2], 1994 Tokyo Workshop [3]). For the workshops, HSVA/Dyne tanker and Series 60 models were used for the validation of the numerical methods and turbulence models. However, those hull forms are quite different from the modern hull forms of actual ships today. It is not easy to apply computational tools to a modern practical hull form with bow and stern bulbs, since they require well-defined hull surface mesh and field grid system for the implementation of numerical methods. This procedure, called pre-processing, is the most time-consuming task in the application of CFD techniques to the hull form evaluation. The main difficulty would be the generation of surface mesh based on offset table, since the information of the hull form given to CFD tools in the initial design process is not a nicely defined NURBS surface but a simple offset table from hull form variation tools.

Grid generation is still the biggest obstacle to the practical use of viscous flow methods. The successful application of the computational tool to the design of hull form depends upon user-friendliness as well as accuracy. An easy and reliable generation of hull surface mesh and field grid is essential for the efficient application of computational tools to hull form design.

To cope with the aforementioned request, a hull surface mesh generation method based on given station offsets along with the stern and bow profiles has been developed. This new method employs non-uniform parametric spline with predetermined waterline end-shapes. It can generate hull surface meshes very quickly, starting from a given offset table. The surface mesh topology chosen in the present study, to present the hull surface with bulbous bow and stern bulb, can be transformed into a rectangle. It implies that flow solvers are able to accommodate the mesh easily and their own accuracy does not deteriorate especially when turbulent quantities are determined on the so-called wall coordinate. A three-dimensional Poisson equation is solved to make up the field grid system, based on the extended Sorenson's method [4]. Utilising the generated surface meshes as boundary grids, the Poisson equation is solved to constitute the field grid system of O–O or O–H topology. Sorenson's method is extended into three dimension to determine grid-control functions. Weighted trans-finite interpolation is also utilised to specify a better initial guess and to make the smooth transition of 3D grids into 2D boundary grids.

One of the main conclusions drawn in the preceding workshops is that the turbulence model is a key in predicting nominal wake distribution at the propeller plane correctly. The higher order turbulence closure of solving differential equations for Reynolds stresses is commonly recommended to simulate wake flow with strong secondary flow like bilge vortices. However, it would be very difficult for ship designers to manage such a complicated model requiring big computational efforts. If the CFD tools are to be utilised in the initial design process, the computational cost should be inexpensive. For that purpose, cost-effective two-equation turbulence models are good candidates for quick hull form evaluation if they can predict stern flow within acceptable accuracy.

The Reynolds-averaged Navier–Stokes equations for turbulent flows around model ships are solved using the cell-centred finite-volume scheme. Several variations of the two-equation turbulence model, such as the standard k–ε model (hereafter SKE), the RNG-based k–ε model (RNG), and the realisable k–ε model (RKE), are tested to identify the stern flow difference caused by the turbulence model. The calculations are performed for the two modern very large crude-oil carriers (VLCC) models with the scale ratio of 1/58 and the calculated results are compared to the experimental data measured in the KRISO towing tank [5]. The two

VLCC hull forms have the same forebody (F1) and the slightly different afterbodies (A1 and A2), namely, KRISO 300K VLCC F1+A1 (hereafter, KVLCC) and F1+A2 (KVLCC2), respectively. An important issue on the performance of the turbulence model for the wake prediction is addressed. Focus is also laid upon whether CFD can correctly tell the difference of flow field due to the slight hull form change. In the following the details of pre-processor, computational modelling and calculated results are described. It is interesting to see that the CFD with relatively simple turbulence closure can tell the stern flow difference quantitatively as well as qualitatively for the two hull forms with frame line modification.

2. GRID GENERATION

2.1. Surface mesh generation

CFD can be a very useful tool to evaluate the performance of a new hull form reliably and quickly. However, the bottleneck exists in preparing surface mesh for the implementation of well-developed flow solvers. It is cumbersome to describe a modern hull form by using only the offset table, since the complexity of bow and stern shapes require more information. If the construction of the ship is considered, the very fine definition of hull form will be needed. However, it should be noted that at most 2000–4000 meshes for hull surface are used for the flow calculation. To present a hull form and to generate surface mesh quickly, the usability is emphasised in the newly developed method. In the present study, commercial ships such as tanker, bulk carrier, and container ship with bow and stern bulb are considered, although the same procedures can be applied to other hull forms. The procedures of surface mesh generation are described in the sequel.

First of all, three-dimensional space curves are presented by using non-uniform parametric spline with the slope controlled at any given points. The parameter chosen for interpolation is the accumulated chord length. The Ferguson basis, utilising position vectors and tangent vectors at the ends, are chosen since it is easy to handle the discontinuities of slope or curvature existing in hull surface profiles [6]. If the curvature or slope at the point is not specified from the offset table, the cubic spline curves are implemented. The procedure begins with an offset table provided by the designer. It usually contains 10–30 offset points at 25 –30 stations with bow and stern profiles. The first step is identifying the offset points having a discontinuous slope or curvature. Then non-uniform parametric spline is utilised to generate sufficiently many interpolated points for the body plan and the side profile. The generated points on the body plan and centreline profile shown in Figure 1, are utilised for generating waterlines. The examples are given for a modern container ship hull form, since big bulbs of the container ship make surface mesh generation more difficult than full form tanker cases.

It is necessary to make up additional station offsets in the bow and stern region to construct a complicated bow and stern shape. At first, waterlines are defined to specify additional station offsets, but the shapes of waterline ending are not clarified in the original station offset. In the present study, the end shapes of waterline near the bow and the stern are defined by using the predetermined parameters, which choose waterline endings from natural spline, normal spline, ellipse, parabola, hyperbola, and their combination. Generated waterlines near the bow and the stern are given in Figure 2. Elliptic waterline ending is usually proper for the bow bulb of the container ship, while hyperbolic ending is suitable for the bulbous bow of VLCC.
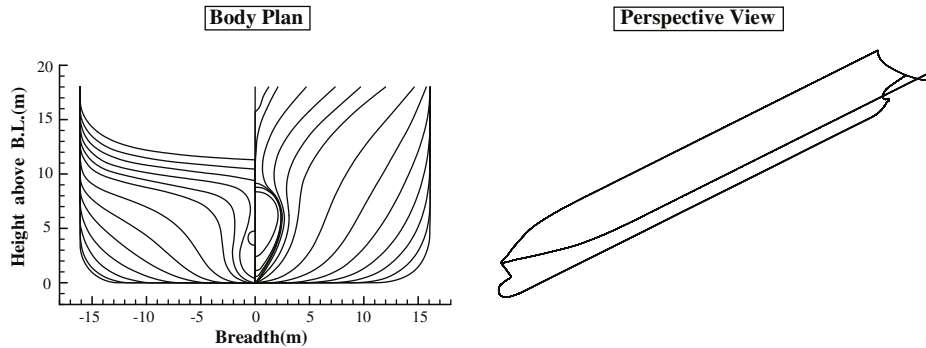
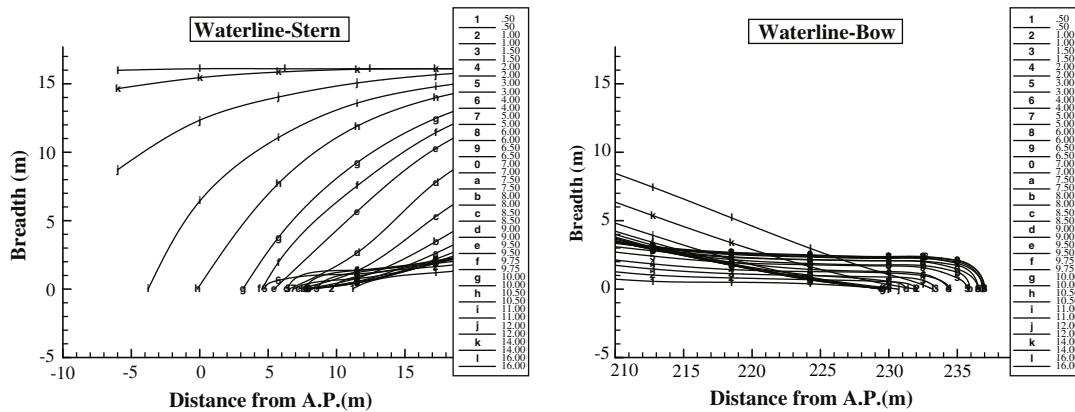Figure 1. Body plan and perspective view of a container ship.

Figure 2. Generated waterlines around the bow and stern of a container ship.

After the waterlines are obtained, dense additional stations near bow and stern are generated using the waterline intersection points at the constant longitudinal locations. These additional station offsets carry the information on complex stern and bow shapes.

In the present study the boundary of mesh topology constitutes keel line, design waterline, bow and stern contours. The generated surface meshes can be transformed into a rectangular domain, which provides the simplicity of application to flow solvers. For a viscous solver, it is crucial to contour the bow and stern profiles into a grid line, since they are lines of flow attachment and detachment, respectively. Furthermore, flow fields near bow and stern region will determine form drag and wake distribution at the propeller plane. When the wave generation on the free surface is included, the aforementioned surface mesh topology will allow the easier modification of hull surface meshes adapting the free surface deformation.

To make the surface mesh flexible, the longitudinal and transverse distribution can be arbitrarily adjusted with the girth length ratio. Once the transverse distribution is given, grid nodes at each station can be found, utilising the length ratio of dense station curves. The nodes at the same transverse ratio, as shown in Figure 3, are connected to complete the longitudinal grid lines. The longitudinal distribution ratio will finally provide the hull surface mesh. It is
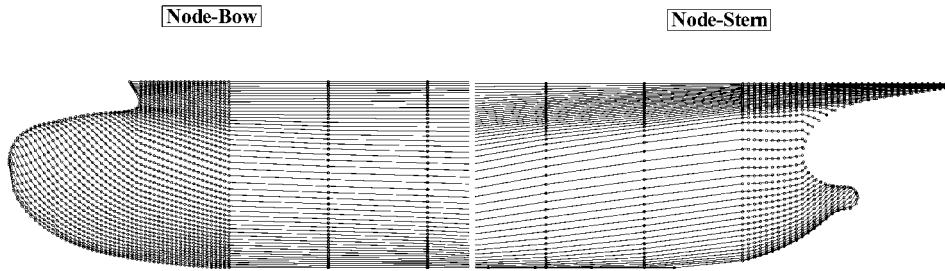
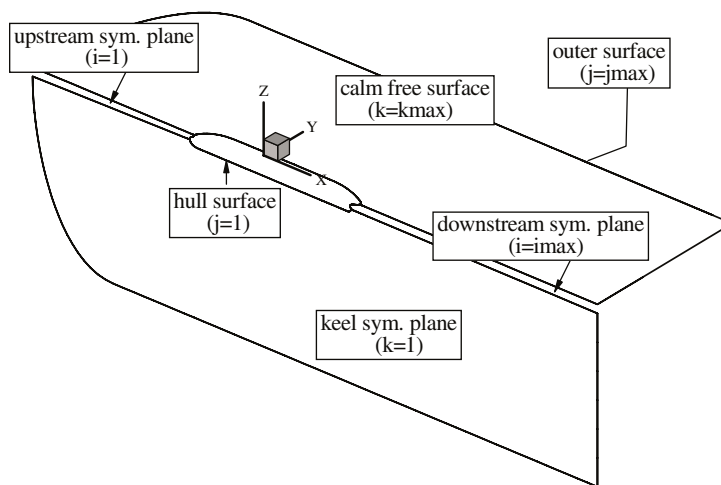Figure 3. Node points to generated surface meshes.

Figure 4. O–O grid topology to calculate viscous flow around a ship.

noteworthy that all the above procedures can be completed within one minute on PC when the original offset table is given. This efficient hull surface mesh generator will facilitate the usability of computational tools for the hull form evaluation during the optimisation process.

2.2. Field grid generation

As described in the previous section, the surface mesh contouring bow and stern profile constitutes one boundary surface of a three-dimensional field grid system for viscous flow calculation. To implement the turbulence model and near-wall specifications for high Reynolds number flow, it is necessary to determine the distance and intersecting angles of the first grid points off the wall. With the aid of O–O topology of the field grid system and the surface mesh contouring bow and stern profiles, the above requirement can be easily satisfied. Figure 4 shows the schematic of O–O grid topology and the coordinate system employed in the present study.

Among six boundary surfaces, the hull surface mesh is already given and the outer surface mesh can be defined algebraically. The two-dimensional grid systems on four other planes

of symmetry are obtained by solving 2D Poisson equation. After constituting six boundary surfaces, it is possible to use the algebraic method like trans-finite interpolation (TFI) to fill out the interior grid system. It is rather simple, but does not guarantee the normality of grid on the hull surface. In the present study three-dimensional Poisson equation is solved to meet the requirement of grid orthogonality and controllability. Sorenson's method, known as GRAPE [4], is extended into three-dimension to define the grid-controlling function of Poisson equation.

The Cartesian coordinate system (x, y, z) in Figure 4 is transformed into computational domain (ξ, η, ζ) and the Poisson equation for grid generation is given by

$$\nabla^2 \xi = f^1, \qquad \nabla^2 \eta = f^2, \qquad \nabla^2 \zeta = f^3 \tag{1}$$

where (f^1, f^2, f^3) are grid control functions in (ξ, η, ζ) directions, respectively. After exchanging dependent and independent variables [7], the equation can be written as

$$g^{11} x_{\xi\xi}^m + g^{22} x_{\eta\eta}^m + g^{33} x_{\zeta\zeta}^m + 2g^{12} x_{\xi\eta}^m + 2g^{13} x_{\xi\zeta}^m + 2g^{23} x_{\eta\zeta}^m + f^1 x_{\xi}^m + f^2 x_{\eta}^m + f^3 x_{\zeta}^m = 0 \tag{2}$$

where x^m represents (x, y, z), respectively, when $m = 1, 2, 3$. The metric coefficient g^{ij} is the dot product of contravariant base vector, as given below.

$$g^{ij} = \hat{a}^i \cdot \hat{a}^j = \xi_x^i \xi_x^j + \xi_y^i \xi_y^j + \xi_z^i \xi_z^j \tag{3}$$

where $\hat{a}^i = \nabla \xi^i = (\xi_x^i, \xi_y^i, \xi_z^i)$ is the contravariant base vector in $\xi^i \ [=(\xi, \eta, \zeta)]$ direction, while the covariant base vectors are defined by $\hat{a}_j = [\partial(x, y, z)]/[\partial \xi^j] = (x_{\xi^j}, y_{\xi^j}, z_{\xi^j})$. These two base vectors form the reciprocal base vectors, i.e., $\hat{a}^i \cdot \hat{a}_j = \delta_j^i$, where δ_j^i is Kronecker delta. The covariant metric coefficient can be determined by

$$g_{ij} = \hat{a}_i \cdot \hat{a}_j = x_{\xi^i} x_{\xi^j} + y_{\xi^i} y_{\xi^j} + z_{\xi^i} z_{\xi^j} \tag{4}$$

To solve Poisson Equation (2), the grid control function (f^1, f^2, f^3) should be defined to meet the requirement of grid system, such as the grid spacing and intersecting angle. Sorenson [4] proposed a definition of grid control function by using the position of the first grid point on two facing boundaries in the 2D plane. In the present study his method is extended into 3D space to specify the grid control function on the hull surface and outer boundary surface.

Let P in Figure 5 be a point on the hull surface and (ξ, ζ) is a local coordinate on the hull surface, while η denotes to the additional local coordinate out of hull surface. Then, (ξ, η, ζ) represents grid system. Assuming (ξ, ζ) can be considered as a plane near P, when the angle between ξ and ζ axis is θ_{13} given from the surface grid system, we can put a point Q on η axis, i.e., the first grid point off the hull surface. Let η axis have angles θ_{12}, θ_{23} with ξ and ζ axis, respectively and Q_1 is the projected point of Q onto (ξ, ζ) plane. On the other hand, another coordinate η' perpendicular to (ξ, ζ) surface can be defined by using $\nabla \eta$. The third axis ζ' normal to ξ and η' axis can be also determined. Thus, (ξ, η', ζ') constitutes a local orthogonal coordinate system at P. Let r and l be the length of line $\overline{PQ}$ and $\overline{PQ_1}$ and the projection of Q_1 onto ξ axis is Q_2. The angles of $\angle QPQ_1$ and $\angle Q_2PQ_1$ are defined by β and
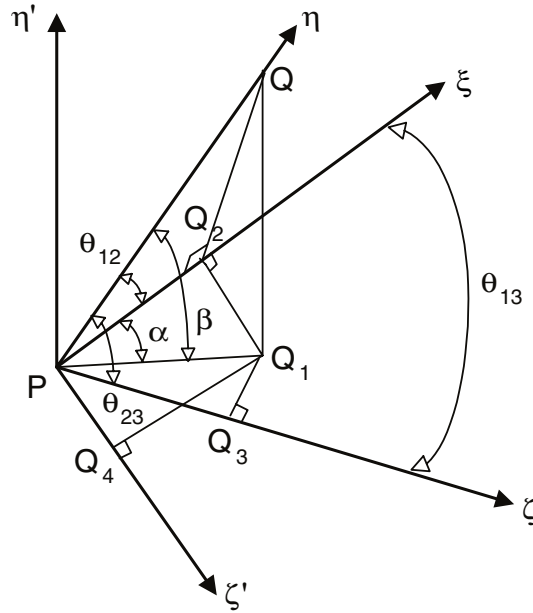
Figure 5. Angle definition in 3D coordinate transformation.

α, respectively. Other geometric relations can be obtained from Figure 5. From geometrical identities, the following equations are deduced.

$$l = r \cos \beta, \quad l \cos \alpha = r \cos \theta_{12}, \quad l \cos(\theta_{13} - \alpha) = r \cos \theta_{23}$$

$$\alpha = \tan^{-1}\left(\frac{-\cos \theta_{12} \cos \theta_{13} + \cos \theta_{23}}{\cos \theta_{12} \sin \theta_{13}}\right) \qquad (5)$$

$$\beta = \cos^{-1}\left(\frac{\cos \theta_{12}}{\cos \alpha}\right)$$

Thus, the point Q can be written in local orthogonal coordinate as $(\xi_Q, \eta'_Q, \zeta'_Q)$, and coordinates can be written by

$$\xi_Q = r \cos \beta \cos \alpha$$
$$\eta'_Q = r \sin \beta \qquad (6)$$
$$\zeta'_Q = r \cos \beta \sin \alpha$$

By using coordinate rotation, the directional cosine of (ξ, η', ζ') with respect to (x, y, z) is given as follows.

$$\hat{e}_{\xi} = \hat{e}_1 = (l_1, m_1, n_1) = \frac{(x_{\xi}, y_{\xi}, z_{\xi})}{\sqrt{x_{\xi}^2 + y_{\xi}^2 + z_{\xi}^2}} = \frac{1}{\sqrt{g_{11}}}(x_{\xi}, y_{\xi}, z_{\xi})$$

$$\hat{e}_{\eta'} = \hat{e}^2 = (l_2, m_2, n_2) = \frac{(\eta_x, \eta_y, \eta_z)}{\sqrt{\eta_x^2 + \eta_y^2 + \eta_z^2}} = \frac{1}{\sqrt{g^{22}}}(\eta_x, \eta_y, \eta_z) \qquad (7)$$

$$\hat{e}_{\zeta'} = \hat{e}_1 \times \hat{e}^2 = (l_3, m_3, n_3) = \frac{1}{\sqrt{g_{11}g^{22}}}(y_{\xi}\eta_z - z_{\xi}\eta_y, z_{\xi}\eta_x - x_{\xi}\eta_z, x_{\xi}\eta_y - y_{\xi}\eta_x)$$

where $(\hat{e}_{\xi'}, \hat{e}_{\eta'}\hat{e}_{\zeta'})$ is unit basis for the local orthogonal coordinates (ξ, η', ζ'), and $\hat{e}_1 = [(\hat{a}_1)/(|\hat{a}_1|)]$, $\hat{e}^2 = [(\hat{a}^2)/(|\hat{a}^2|)]$ are the unit covariant vector in ξ direction and the unit contravariant vector in η direction, respectively. Finally the grid point Q off the hull surface at P with the distance r and the intersecting angles θ_{12} and θ_{23} has the relations

$$\vec{PQ} = (x_{\eta}, y_{\eta}, z_{\eta}) = ([l_1\xi_Q + l_2\eta'_Q + l_3\zeta'_Q], [m_1\xi_Q + m_2\eta'_Q + m_3\zeta'_Q],$$
$$[n_1\xi_Q + n_2\eta'_Q + n_3\zeta'_Q]) \qquad (8)$$

Since $(x_{\eta}, y_{\eta}, z_{\eta})$ is given, in order to obtain the grid control functions at the hull surface point P, we can rewrite the Poisson Equation (2) in the following form,

$$f^1 x_{\xi} + f^2 x_{\eta} + f^3 x_{\zeta} = -g^{11}x_{\xi\xi} - g^{22}x_{\eta\eta} - g^{33}x_{\zeta\zeta} - 2g^{12}x_{\xi\eta} - 2g^{13}x_{\xi\zeta} - 2g^{23}x_{\eta\zeta}$$

$$f^1 y_{\xi} + f^2 y_{\eta} + f^3 y_{\zeta} = -g^{11}y_{\xi\xi} - g^{22}y_{\eta\eta} - g^{33}y_{\zeta\zeta} - 2g^{12}y_{\xi\eta} - 2g^{13}y_{\xi\zeta} - 2g^{23}y_{\eta\zeta} \qquad (9)$$

$$f^1 z_{\xi} + f^2 z_{\eta} + f^3 z_{\zeta} = -g^{11}z_{\xi\xi} - g^{22}z_{\eta\eta} - g^{33}z_{\zeta\zeta} - 2g^{12}z_{\xi\eta} - 2g^{13}z_{\xi\zeta} - 2g^{23}z_{\eta\zeta}$$

On hull surface $(j = 1)$, the terms in the right-hand side can be determined as Sorenson suggested.

$$(x_{\xi\eta})_1 = \tfrac{1}{2}[-3(x_{\xi})_1 + 4(x_{\xi})_2 - (x_{\xi})_3]$$

$$(x_{\eta\eta})_1 = -3.5x_1 + 4x_2 - 0.5x_3 - (x_{\eta})_1, \text{ etc.}$$

The values of grid control functions at hull surface are determined by solving the linear Equation (9) for (f^1, f^2, f^3). If the outer boundary $(j = j_{\max})$ is also to be treated similarly, the grid control functions of domain are defined using the power of index ratio of j in η direction.

$$f^m(i, j, k) = f^m(i, 1, k)\left[1 - \left(\frac{j-1}{j_{\max}-1}\right)\right]^a + f^m(i, j_{\max}, k)\left[\frac{j-1}{j_{\max}-1}\right]^b, \quad m = 1, 2, 3 \qquad (10)$$

where a, b are the exponents for controlling grid expansion rate. With the aid of the above equations, the grid control functions are determined for three-dimensional grid system in the same way as Sorenson's two-dimensional one.

Now Poisson Equation (2) is discretised and solved. Efforts should be paid to insure the robustness of Poisson solver, since the initial guess for the Poisson iterative solver for grid

generation is usually very poor. In the present study the Poisson equation is discretised by using the weighting function scheme [8]. The discretised linear equations are solved by using the modified strongly implicit procedure (MSIP) [9]. The combination of the weighting function scheme and the MSIP linear solver provides the robust and efficient solution of Poisson equation for three-dimensional grid generation.

The algebraic method other than the elliptic method is also a possible tool for grid generation. The most common algebraic method is trans-finite interpolation (TFI). Among several variations of TFI, a weighted TFI scheme of preserving length ratio [10] is adopted for initial guess for Poisson equation to enhance the convergence. The final equation of TFI is given below.

$$
\begin{aligned}
\vec{R}(i,j,k) =& \vec{F}_1(i,j,k) + \vec{F}_2(i,j,k) + \vec{F}_3(i,j,k) \\
\vec{F}_1(i,j,k) =& \vec{R}(1,j,k)[1 - s(i,j,k)] + \vec{R}(i_{\max},j,k)s(i,j,k) \\
\vec{F}_2(i,j,k) =& \{\vec{R}(i,1,k) - \vec{F}_1(i,1,k)\}[1 - t(i,j,k)] \\
& + \{\vec{R}(i,j_{\max},k) - \vec{F}_1(i,j_{\max},k)\}t(i,j,k) \\
\vec{F}_3(i,j,k) =& \{\vec{R}(i,j,1) - \vec{F}_1(i,j,1) - \vec{F}_2(i,j,1)\}[1 - u(i,j,k)] \\
& + \{\vec{R}(i,j,k_{\max}) - \vec{F}_1(i,j,k_{\max}) - \vec{F}_2(i,j,k_{\max})\}u(i,j,k)
\end{aligned}
\tag{11}
$$

where $\vec{R}(i,j,k)$ represents the position vector of grid points $(x(i,j,k),\ y(i,j,k),\ z(i,j,k))$ and blending functions $(s(i,j,k),\ t(i,j,k),\ u(i,j,k))$ in (ξ,η,ζ) direction are given below.

$$
\begin{aligned}
s(i,j,k) =& s(i,1,k)[1 - t(i,j,k)] + s(i,j_{\max},k)t(i,j,k) \\
& + s(i,j,1)[1 - u(i,j,k)] + s(i,j,k_{\max})u(i,j,k) \\
& - s(i,1,1)[1 - t(i,j,k)][1 - u(i,j,k)] \\
& - s(i,j_{\max},1)t(i,j,k)[1 - u(i,j,k)] - s(i,1,k_{\max})[1 - t(i,j,k)]u(i,j,k) \\
& - s(i,j_{\max},k_{\max})t(i,j,k)u(i,j,k) \\
t(i,j,k) =& t(i,j,1)[1 - u(i,j,k)] + t(i,j,k_{\max})u(i,j,k) \\
& + t(1,j,k)[1 - s(i,j,k)] + t(i_{\max},j,k)s(i,j,k) \\
& - t(1,j,1)[1 - u(i,j,k)][1 - s(i,j,k)] \\
& - t(1,j,k_{\max})u(i,j,k)[1 - s(i,j,k)] \\
& - t(i_{\max},j,1)[1 - u(i,j,k)]s(i,j,k) - t(i_{\max},j,k_{\max})u(i,j,k)s(i,j,k) \\
u(i,j,k) =& u(1,j,k)[1 - s(i,j,k)] + u(i_{\max},j,k)s(i,j,k) \\
& + u(i,1,k)[1 - t(i,j,k)] + u(i,j_{\max},k)t(i,j,k) \\
& - u(1,1,k)[1 - s(i,j,k)][1 - t(i,j,k)] \\
& - u(i_{\max},1,k)s(i,j,k)[1 - t(i,j,k)] \\
& - u(1,j_{\max},k)[1 - s(i,j,k)]t(i,j,k) - u(i_{\max},j_{\max},k)s(i,j,k)t(i,j,k)
\end{aligned}
\tag{12}
$$

The above three equations are coupled nonlinear equations which can be solved iteratively. The values at boundary surfaces, e.g., $s(i, 1, k)$ means the integrated length ratio in ξ direction along constant ζ lines on $j = 1$ surface. All the boundary values can be calculated since grid points on six boundary surfaces are already given, *a priori* to three-dimensional field grid generation.

To make the procedure complete, the intersecting angles of the first grid points off the hull surface, i.e., θ_{12}, θ_{23} should be specified at every hull surface points. The orthogonal condition ($\theta_{12} = \theta_{23} = 90°$) can be used, however, the exact normality is sometimes too severe, especially at points near bow and stern. Thus, the mixing ratio of $90°$ and the angles of initial guess by TFI are specified to decide intersecting angles of radial grid lines off the hull surface. It is also noteworthy that the 3D Poisson solution does not smoothly meet the boundary surface grids, since the 2D Poisson equation used for boundary surface grids is not a degeneration of the 3D Poisson equation for the field grid system. To avoid the abrupt change of grid lines near the plane of symmetry boundary surface, the solution of the 3D Poisson equation is blended exponentially with the TFI solution near the 2D boundary surfaces ($i = 1$, $i = i_{max}$, $k = 1$, $k = k_{max}$). The combination of the elliptic and the algebraic grid generation methods provides the field grid system efficiently for viscous flow calculation around a ship.

3. NUMERICAL METHODS

3.1. Governing equations and turbulence models

The governing equations for turbulent flow in the present study are Reynolds-averaged Navier–Stokes equations for momentum transport and the continuity equation for mass conservation. The Cartesian coordinates are used, as shown in Figure 4, where (x, y, z) denotes downstream, starboard, and upward direction, respectively. The origin of the coordinates is located at the midship and calm free surface. All the quantities are non-dimensionalised by the speed (V) and the length between perpendiculars (L_{pp}) of model ship, and fluid density (ρ).

Continuity equation:

$$\frac{\partial u_k}{\partial x_k} = 0 \tag{13}$$

Momentum transport equation:

$$\frac{\partial u_i}{\partial t} + \frac{\partial (u_i u_j)}{\partial x_j} = -\frac{\partial p}{\partial x_i} + \frac{\partial \tau_{ij}}{\partial x_j} \tag{14}$$

where $u_i = (u, v, w)$ are velocity components in $x_i = (x, y, z)$ directions, while p is static pressure. Stress tensor τ_{ij} can be written using Boussinesq's isotropic eddy viscosity hypothesis as follows.

$$\tau_{ij} = v_e \left(\frac{\partial u_i}{\partial x_j} + \frac{\partial u_j}{\partial x_i} \right) - \frac{2}{3} \delta_{ij} k \tag{15}$$

Here, k is turbulent kinetic energy and v_e is effective viscosity, i.e., the sum of turbulent eddy viscosity (v_t) and molecular kinematic viscosity (v).

$$v_e = v_t + \frac{1}{R_e} \tag{16}$$

and Re is Reynolds number (VL_{pp}/v).

For turbulence closure, three k–ε models are utilised. Those are the standard k–ε model (SKE) [11], the RNG-based k–ε model (RNG) [12], and the realisable k–ε model (RKE) [13]. With the k–ε turbulence model, the eddy viscosity v_t can be written as

$$v_t = C_\mu \frac{k^2}{\varepsilon} \tag{17}$$

In the standard k–ε model (SKE) $C_\mu = 0.09$, while in the RNG-based model (RNG) $C_\mu = 0.085$. For the realisable model (RKE) C_μ has rather complicated form given in the followings.

$$C_\mu = \frac{1}{A_0 + A_S \dfrac{U^* k}{\varepsilon}} \tag{18}$$

where the terms are defined as

$$U^* = \sqrt{S_{ij} S_{ij} + \Omega_{ij} \Omega_{ij}}$$

$$S_{ij} = \frac{1}{2}\left(\frac{\partial u_i}{\partial x_j} + \frac{\partial u_j}{\partial x_i}\right)$$

$$\Omega_{ij} = \frac{1}{2}\left(\frac{\partial u_i}{\partial x_j} - \frac{\partial u_j}{\partial x_i}\right)$$

$$A_0 = 4.0, \quad A_S = \sqrt{6}\cos\phi$$

$$\phi = \frac{1}{3}\arccos(\sqrt{6}W)$$

$$W = \frac{S_{ij} S_{jk} S_{ki}}{\tilde{S}^3}, \quad \tilde{S} = \sqrt{S_{ij} S_{ij}}$$

Turbulent kinetic energy k can be obtained by the solution of the following transport equation. For all three k–ε models, equation for k has the same form as given by the following.

Turbulent kinetic energy transport equation:

$$\frac{\partial k}{\partial t} + \frac{\partial (u_j k)}{\partial x_j} = \frac{\partial}{\partial x_j}\left[\left(v + \frac{v_t}{\sigma_k}\right)\frac{\partial k}{\partial x_j}\right] + G - \varepsilon \tag{19}$$

where ε represents the dissipation rate of turbulent kinetic energy and G is production term as given below.

$$G = v_t \left(\frac{\partial u_i}{\partial x_j} + \frac{\partial u_j}{\partial x_i}\right)\frac{\partial u_i}{\partial x_j} \tag{20}$$

In the standard k–ε model (SKE) and the realisable k–ε model (RKE), $\sigma_k = 1.0$, while in the RNG-based model (RNG) $\sigma_k = 0.719$.

Transport equation for dissipation rate ε is written by the following.

Equation for dissipation rate of turbulent kinetic energy:

$$\frac{\partial \varepsilon}{\partial t} + \frac{\partial (u_j \varepsilon)}{\partial x_j} = \frac{\partial}{\partial x_j}\left[\left(v + \frac{v_t}{\sigma_\varepsilon}\right)\frac{\partial \varepsilon}{\partial x_j}\right] + S_\varepsilon \tag{21}$$

In SKE and RNG,

$$S_\varepsilon = C_{\varepsilon 1}\frac{\varepsilon}{k}G - C_{\varepsilon 2}\frac{\varepsilon^2}{k}$$

where for SKE, $\sigma_\varepsilon = 1.3$, $C_{\varepsilon 1} = 1.44$, and $C_{\varepsilon 2} = 1.92$, while for RNG, $\sigma_\varepsilon = 0.719$, $C_{\varepsilon 1} = 1.42$, and $C_{\varepsilon 2}$ is given by

$$C_{\varepsilon 2} = 1.68 + \frac{C_\mu \eta^3(1 - \eta/4.38)}{1 + 0.012\eta^3}$$

where $\eta = S\dfrac{k}{\varepsilon}$, $S = \sqrt{2S_{ij}S_{ij}}$.

In RKE,

$$S_\varepsilon = C_{\varepsilon 1}S\varepsilon - C_{\varepsilon 2}\frac{\varepsilon^2}{k + \sqrt{v\varepsilon}}$$

where $\sigma_\varepsilon = 1.2$, $C_{\varepsilon 2} = 1.9$, and

$$C_{\varepsilon 1} = \max\left(0.43, \frac{\eta}{\eta + 5}\right)$$

It is advisory to use a near-wall turbulence model to resolve boundary layer up to the wall, however, the number of grids should be almost doubled. For the present study the so-called Launder and Spalding's wall function [11] is utilised to bridge the fully turbulent region and the wall. The first grid point in the wall function approach is approximately 100 times off the wall compared to that in the near wall turbulence model. It provides the economy and robustness to a viscous flow calculation method as a design tool. Since the flow around a ship is of the present interest, the so-called singular separation with flow reversal is not expected, although the formation of longitudinal vortex is often observed. The wall function is known to give good results for such a mild flow. The wall function adopted in the present calculation is given by the following.

Launder and spalding's wall function:

$$\frac{U_P C_\mu^{1/4} k_P^{1/2}}{\tau_w} = \frac{1}{\kappa}\ln(En_P^*)$$
$$\kappa = 0.41, \quad E = 8.342 \tag{22}$$

where τ_w is wall shear stress, U_P and k_P are the magnitude of velocity and turbulent kinetic energy at the center of the first cell off the wall. The non-dimensionalised normal distance

from the wall n_P^* is given by

$$n_P^* = \frac{C_\mu^{1/4} k_P^{1/2} n_P}{\nu}$$

Generation of turbulent kinetic energy at the first cell off the wall is given as follows.

$$\bar{G}_P = \tau_w \left(\frac{\partial U}{\partial n}\right)_P = \frac{\tau_w^2}{\kappa C_\mu^{1/4} k_P^{1/2} n_P}$$

while dissipation at that cell is written by

$$\bar{\varepsilon}_P = \frac{C_\mu^{3/4} k_P^{3/2}}{\kappa n_P}$$

3.2. Discretisation

The cell-centred finite-volume method is utilised to discretise governing equations, as discussed in Ferziger and Peric [15]. Governing equations are integrated over a grid cell Ω with boundary surface S, resulting in the following equations.

$$\int_S \vec{v} \cdot \vec{n} \, dS = 0 \tag{23}$$

$$\frac{\partial}{\partial t} \int_\Omega u_i \, d\Omega + \int_S u_i \vec{v} \cdot \vec{n} \, dS = \int_S \tau_{ij} \vec{i}_j \cdot \vec{n} \, dS - \int_S p \vec{i}_i \cdot \vec{n} \, dS \tag{24}$$

where $\vec{i}_j$ is unit vector in x_j-direction.

The first term of momentum transport equation, temporal derivative is ignored by putting very big time step, since only the steady solution is of the present interest. Convection terms are discretised using QUICK scheme of the third order. But the QUICK scheme requires 13 point stencil, resulting in complicated algebraic equations. Thus, the so-called deferred correction is adopted, which a simple upwind scheme is used with lagged higher order terms. The deferred correction makes a seven point stencil with simple linear equations.

Rewriting the third term of the stress tensor,

$$\int_S \tau_{ij} \vec{i}_j \cdot \vec{n} \, dS = \int_S \nu_t \left(\frac{\partial u_i}{\partial x_j} + \frac{\partial u_j}{\partial x_i}\right) \vec{i}_j \cdot \vec{n} \, dS = \int_S \nu_t \left(\text{grad}(u_i) \cdot \vec{n} + \frac{\partial u_j}{\partial x_i} \vec{i}_j \cdot \vec{n}\right) ds \tag{25}$$

The central difference scheme is utilised for diffusion terms, while the terms coming from grid non-orthogonality is deferred. Linear equations obtained from the seven point stencil are solved using a strongly implicit procedure.

If the pressure field is known *a priori*, momentum equations will give the correct velocity field. However, those velocity components will not satisfy the continuity equation. To ensure a divergence-free velocity field, the SIMPLEC method is employed. Since the collocated grid arrangement is chosen, the artificial dissipation term in pressure correction equation is added, as discussed in Ferziger and Peric [15]. The resulting linear equations for pressure correction are solved using a strongly implicit procedure until the equation residual drops by an order of magnitude for each iteration.

To complete the solution procedures, at first, hull surface meshes are generated as mentioned in Section 2.1. Taking the generated surface mesh as a boundary grid surface, three-dimensional field grids are obtained following the method given in Section 2.2. With the generated grid system, flow calculation is initiated, starting from uniform stream. With the grids and initial guess for flow field ready, iteration begins for coupled partial differential equations. After three momentum-transport equations are solved sequentially to obtain preliminary velocity components, the pressure correction equations are solved to get pressure field. Then, velocity components are corrected using new pressure values. Then, turbulence equations are solved and eddy viscosity is updated. Iteration continues until total residuals of each momentum equation are less than 10^{-5}, which is about five orders less than the initial residuals.

4. RESULTS

4.1. Test hull forms

To confirm the usability of the developed numerical method, it should be validated to the experimental data. However, the reliable data containing three-dimensional velocity fields around a realistic hull form are very rare, since they are usually owned by shipbuilding companies. Recently measured flow fields around two modern VLCC models of 300,000 DWT are provided [5] for the validation of CFD application for the prediction of the boundary layer and wake at the stern region of full form tankers in towing tank model scale. Two hull forms with the same forebody (F1) and slightly different afterbody geometries (A1 and A2) having the same side profile were designed and used for the local flow measurement. The two VLCC hull forms, i.e., KRISO 300K VLCC F1 + A1 and F1 + A2 are named by KVLCC and KVLCC2, respectively. The first VLCC stern hull form (A1) had barge-type stern frame lines with fine stern-end bulb, while the second stern hull form (A2) had more U-shaped stern frame lines than the first one, as shown in Figure 6. The principal particulars of the VLCC hull forms are given in Table I. The hull form changes of VLCC sterns (A1 and A2) was as much as the shipyards usually apply, which ensured the usefulness of measured data in the evaluation of CFD tools for wake prediction.

The measurements were carried out at six stern stations (St. 3, 2, 1, 0.35, $-0.4525, -2$) of $x = 0.35$, 0.4, 0.45, 0.4825, 0.5226, and 0.6 of both KVLCC and KVLCC2 model ships with the scale ratio of 1/58. In the shipbuilding engineering, St. 0 and St. 20 mean the after perpendicular (AP) at the stern, and the forward perpendicular (FP) at bow of a ship, respectively. All the local flow measurements in the towing tank were performed in the
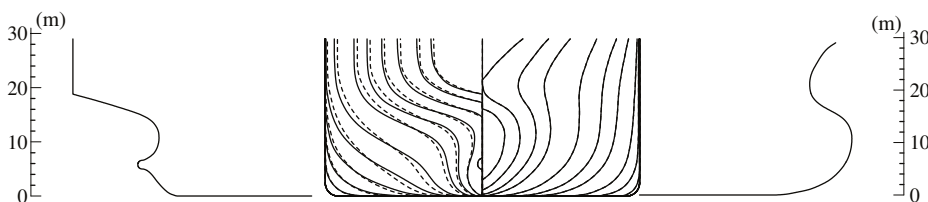

Figure 6. Body plans and side profile of KVLCC and KVLCC2 (solid: KVLCC, dashed: KVLCC2).

Table I. Principal particulars of KVLCC and KVLCC2.

Ship	KVLCC		KVLCC2	
Designation	Prototype	Model	Prototype	Model
Scale ratio	1.0	1/58.0	1.0	1/58.0
Speed (ms^{-1})	7.9739	1.047	7.9739	1.047
Froude Number (*Fn*)	0.142	0.142	0.142	0.142
Reynolds number (*Re*)	2.1×10^9	4.6×10^6	2.1×10^9	4.6×10^6
Length (m)	320.0	5.5172	320.0	5.5172
Breadth (m)	58.0	1.0	58.0	1.0
Depth (m)	30.0	0.5172	30.0	0.5172
Draft (m)	20.8	0.3586	20.8	0.3586
Wetted surface area (m^2)	27 320.0	8.1213	27 194.0	8.0838
Displacement (m^3)	312 737	1.6029	312 621	1.6023
Block coefficient (CB)	0.8101	0.8101	0.8098	0.8098
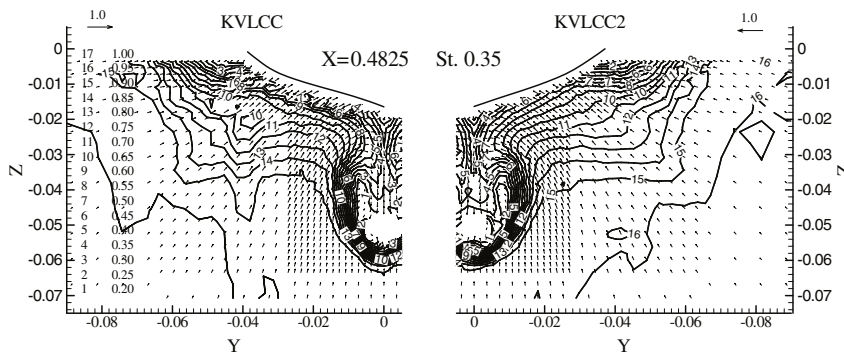
Figure 7. Measured mean velocity fields at $x = 0.4825$ (left: KVLCC, right: KVLCC2).

fixed condition, where neither trim nor sinkage was allowed. The propeller plane ($x = 0.4825$, St. 0.35) is located just behind the stern cap. The shaft centreline of the VLCCs is located at $z = -0.04688$. The local flow measurement in the towing tank was performed at the Reynolds number of 4.6×10^6, while the corresponding Froude number was 0.142. The effect of free surface is ignored because of low Froude number in the present calculation. Instead, the Neumann condition was used for the symmetric free surface. Focus is laid upon the prediction of nominal wake distribution at the propeller plane, since it is the most important information from the viscous flow calculation for the design of propeller. Figure 7 shows measured mean velocity fields around two VLCC ship models at $x = 0.4825$, where the propeller would be located. It is observed that wake contours are more of a circular shape and have a stronger hook for KVLCC2. Details of wake distribution will be discussed later along with calculated results.
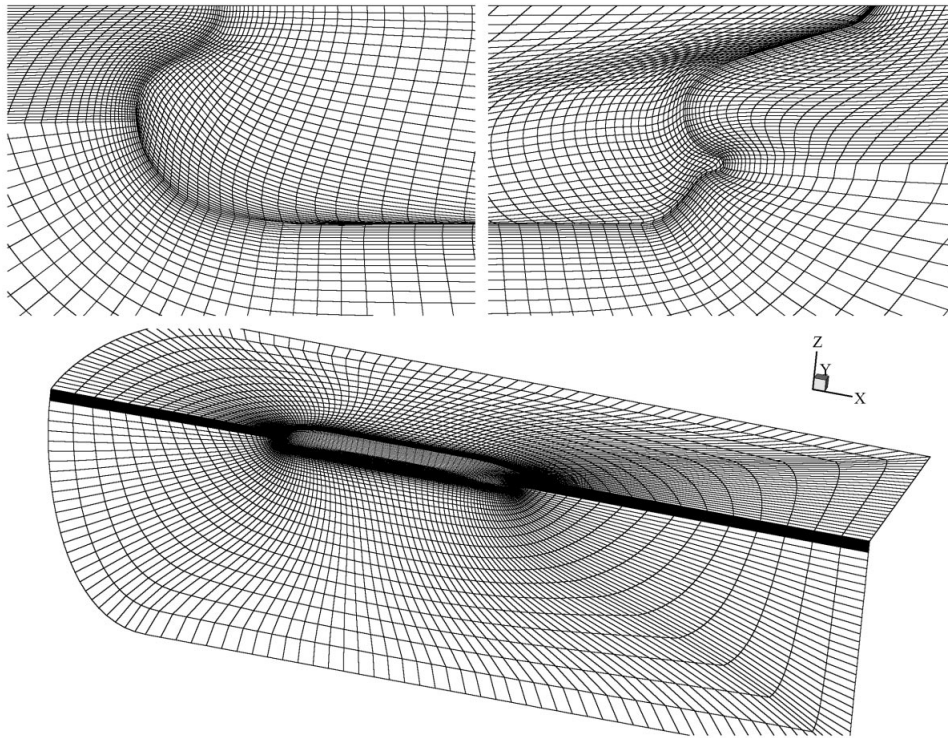
Figure 8. Generated grids with O–O topology around KVLCC.

4.2. Grid dependency

For the present calculation, three grid systems of $83 \times 33 \times 33$, $99 \times 41 \times 41$, and $117 \times 49 \times 49$ grids with O–O grid topology are used to investigate grid dependence of the solution. It should be mentioned that KVLCC and KVLCC2 hull forms have transom below the calm free surface, thus transom is artificially closed by extending the side profiles. Figure 8 displays a $99 \times 41 \times 41$ grid system around KVLCC. Calculated drag coefficients with RKE are 3.802×10^{-3}, 3.830×10^{-3}, 3.835×10^{-3} for $83 \times 33 \times 33$, $99 \times 41 \times 41$, $117 \times 49 \times 49$. grids, respectively. Predicted wake distributions at the propeller plane are compared for three different grid levels in Figure 9. It was found that the calculated result with $99 \times 41 \times 41$ grids is almost the same as that with $117 \times 49 \times 49$ grids. Radial distributions of circumferentially averaged axial velocity components at the propeller plane are compared in Figure 10. As already shown in Figure 9, the calculated wake distribution with $99 \times 41 \times 41$ and $117 \times 49 \times 49$ grids are very similar. It is noteworthy that less than 2 h in a single processor of Pentium-III 500 MHz were required to get convergence up to five orders of magnitude less residuals with $99 \times 41 \times 41$ grids.

In the present study O–O grid topology was adopted. To explore the difference caused by grid topology, O–H grid system with $160 \times 41 \times 41$ is generated as shown in Figure 11. It should be noted that the number of grids on the hull surface is the same as the previous
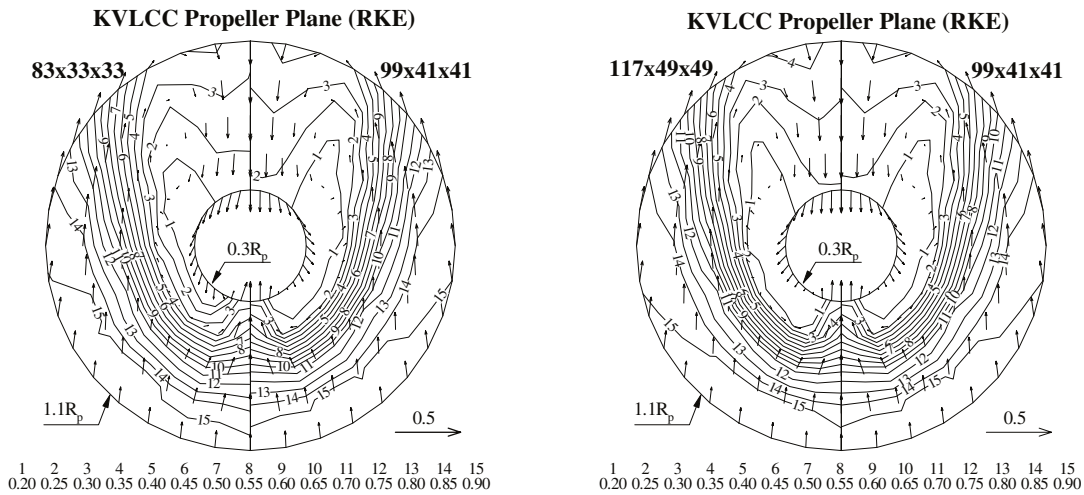
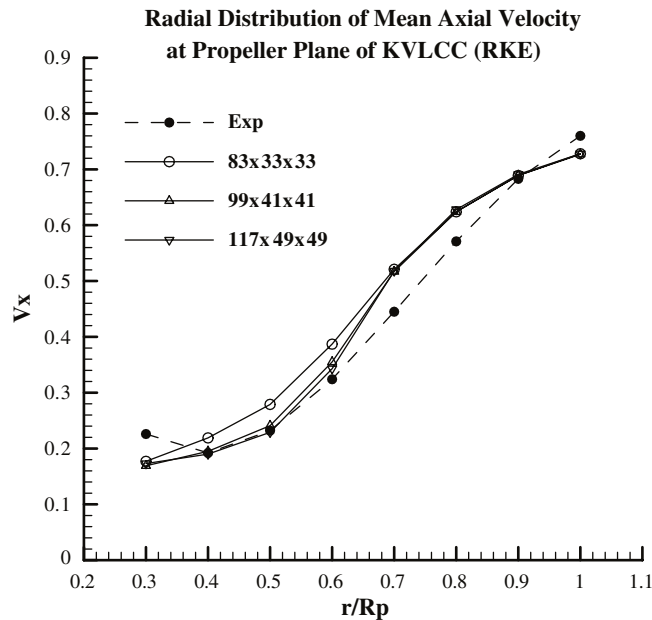Figure 9. Wake prediction of KVLCC with three different grid levels (O–O topology).

Figure 10. Radial distribution of circumferentially averaged axial velocity components at propeller plane with three different grid levels (O–O topology).

$99 \times 41 \times 41$ grids in O–O topology. Figure 12[t] shows the comparison of propeller plane wake of KVLCC with O–O and O–H topology. Calculated surface pressure distributions are given in Figure 13 for both grid topologies. For O–H topology, transom stern is not
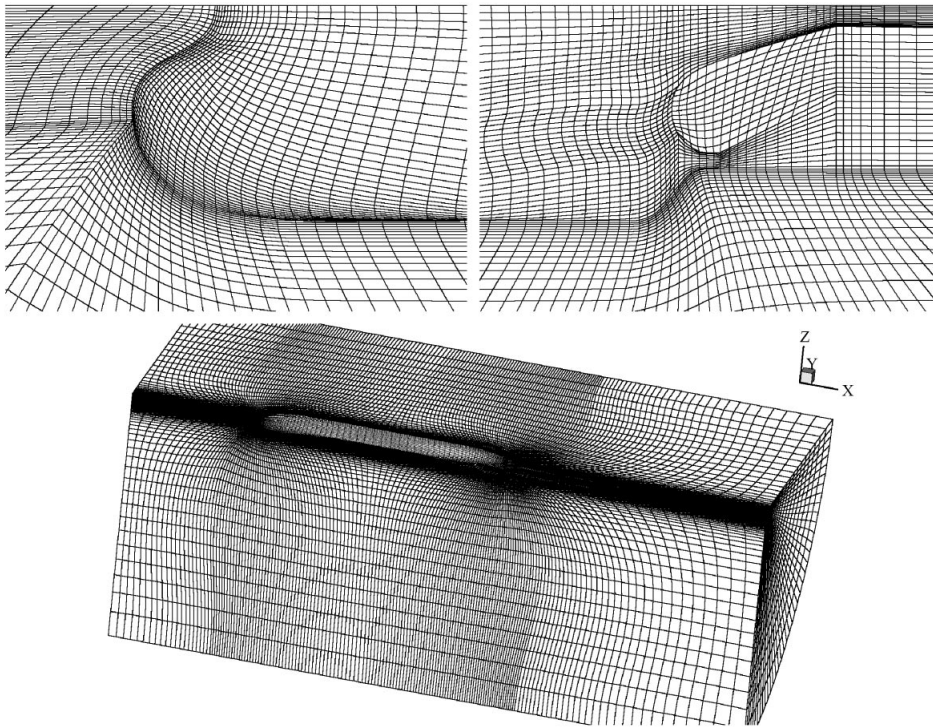
Figure 11. Generated grids with O–H topology around KVLCC.

extended to confirm that extending transom profiles in O–O topology did not affect the solution at the propeller plane. It was observed that both topologies provided very similar results. In the following the calculated results with $99 \times 41 \times 41$ grids in O–O grid topology will be discussed.

4.3. Turbulence model evaluation

The previous workshop on viscous flow calculation around ships pointed out that the turbulence modelling is a key to predict accurately the wake distribution at the propeller plane. ITTC committee [1] also suggests that turbulence model is important in utilising CFD for hull form design, especially for the prediction of bilge vortex and wake in the stern region of full form tankers.

The higher order turbulence closure such as Reynolds stress model is desirable to simulate wake flow with bilge vortices. However, the Reynolds stress models are too expensive for the routine design process of hull form. Thus, in the present study, $k-\varepsilon$ turbulence models are evaluated, since they are still the best for the engineering application. In the followings, for KVLCC, the results with three different $k-\varepsilon$ turbulence models are discussed to investigate the effect of turbulence model on flow prediction.
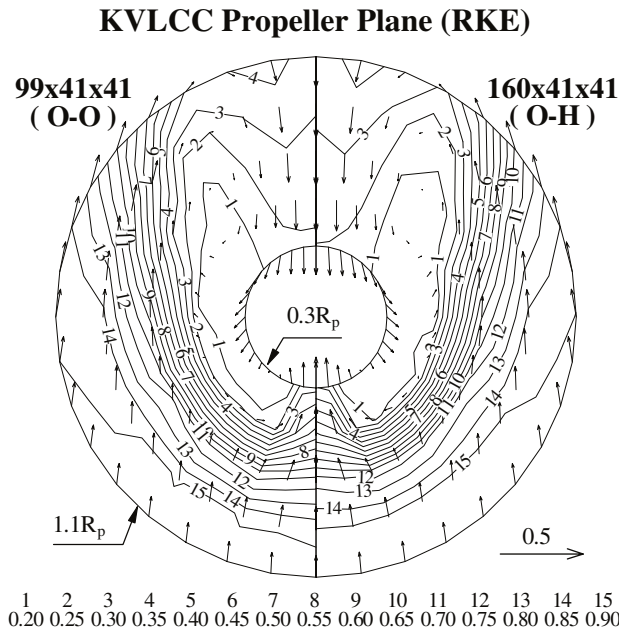
KVLCC Propeller Plane (RKE)

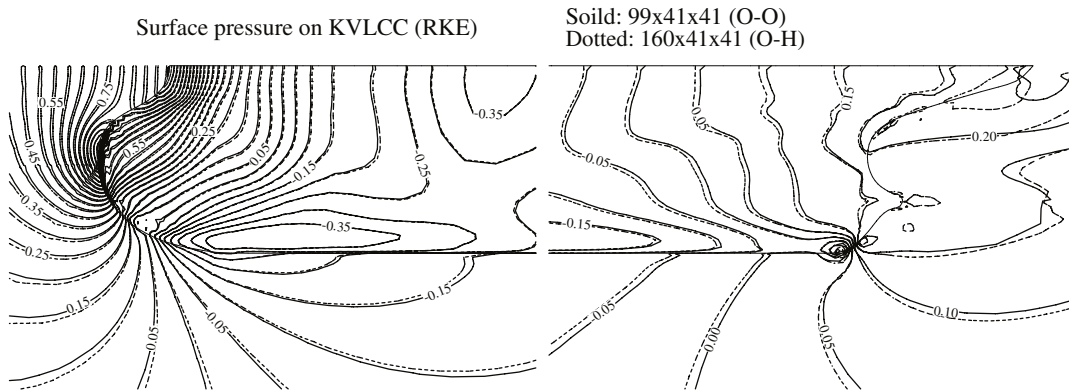Figure 12. Wake prediction of KVLCC with O–O and O–H topology (left: O–O, right: O–H).

Figure 13. Surface pressure distribution on KVLCC (solid: O–O topology, dashed: O–H topology).

In Figures 14–16, calculated velocity fields with SKE, RNG, and RKE are compared to experiments at $x = 0.4$ and 0.4825 (i.e., St. 2 and 0.35). The calculated results with SKE show a thicker boundary layer at $x = 0.4$, while little bilge vortices are found at the propeller plane. For RNG, boundary layer thickness is predicted better, however, the RNG-based $k–\varepsilon$ model still failed to predict distortion of axial velocity contours at the propeller plane. On the other hand, the realisable $k–\varepsilon$ model (RKE) provides the correct boundary layer thickness with hook-like distortion of axial velocity contours. It is rather surprising, since the wall function is utilised to
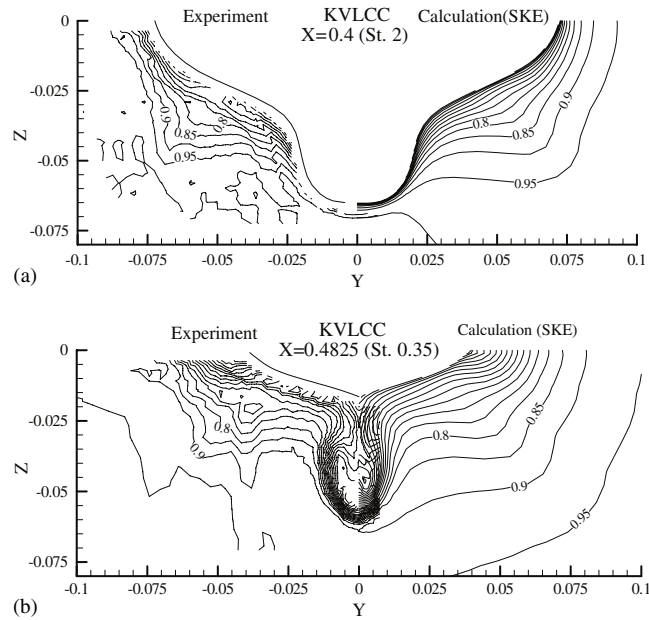
Figure 14. (a) Comparison of longitudinal velocity field at $x = 0.4$ of KVLCC using SKE. (b) Comparison of longitudinal velocity field at $x = 0.4825$ of KVLCC using SKE.
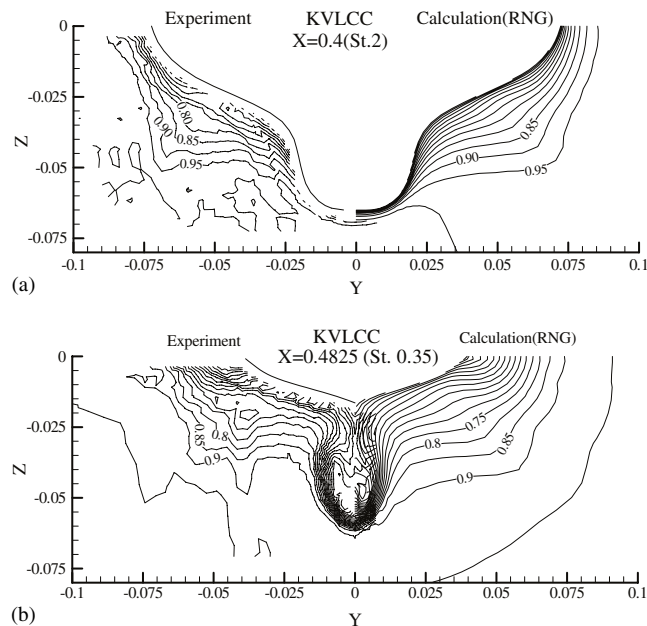

Figure 15. (a) Comparison of longitudinal velocity field at $x = 0.4$ of KVLCC using RNG. (b) Comparison of longitudinal velocity field at $x = 0.4825$ of KVLCC using RNG.
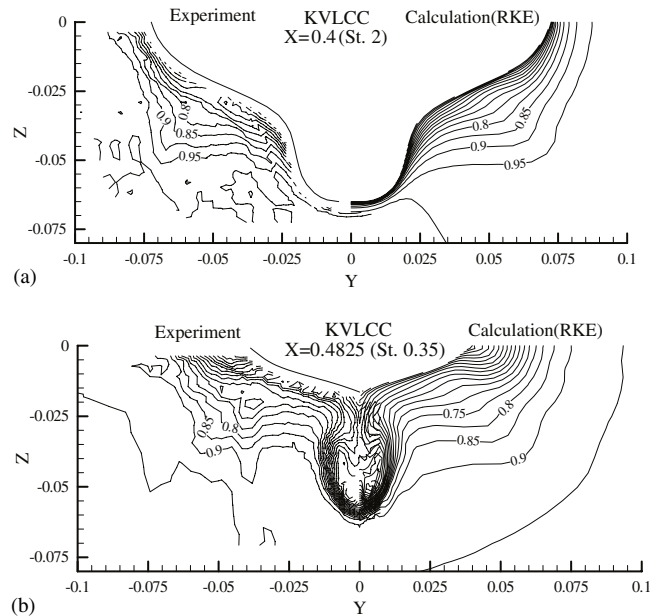
Figure 16. (a) Comparison of longitudinal velocity field at $x = 0.4$ of KVLCC using RKE. (b) Comparison of longitudinal velocity field at $x = 0.4825$ of KVLCC using RKE.

skip the details of near wall turbulence phenomena, as indicated in the previous computational results using a commercial package by Kim [14], who solved flow around the after half-body of HSVA tanker. In Figure 17 propeller plane wakes are compared. As expected from Figures 14 and 15, SKE and RNG failed to predict the hook in U-contours, while RKE succeeded.

Calculated turbulent kinetic energy and eddy viscosity at $x = 0.4825$ are shown in Figures 18 and 19. RNG provided a lower level of turbulence than the others. Eddy viscosity contours of SKE and RNG show similar shapes, as expected from the axial velocity contours. RKE has lower eddy viscosity values than SKE and RNG except at the location above the hub and near the vortex core, where high eddy viscosity is concentrated. These figures might give some clues about RKE having a nice hook-like shape as in Figure 17. It is noteworthy that the coefficient in Equation (18) of RKE is not a constant but a function of mean strain rate and vorticity, and the axial velocity contours with RKE resemble those of eddy viscosity. It would be premature to tell which turbulence model is superior in predicting wake distribution, but RKE seems to have an edge.

Figure 20 shows radial distribution of circumferentially averaged axial velocity components at propeller plane of KVLCC for three turbulence models. As already shown in Figure 17, SKE shows poor results. RNG gives a little better result, but still far from the experiment. However, RKE yields to fairly good agreement with experiments. The discrepancy near the hub $(0.3-0.4 R_P)$ might be coming from the simple extrapolation of velocity fields of the experiment, since the measured local flow angles are out of calibration range beneath the hub, thus, discarded in the experiment. If the velocity distribution outside of $0.5 R_P$ is considered, RKE gives directly applicable results, which is very encouraging.
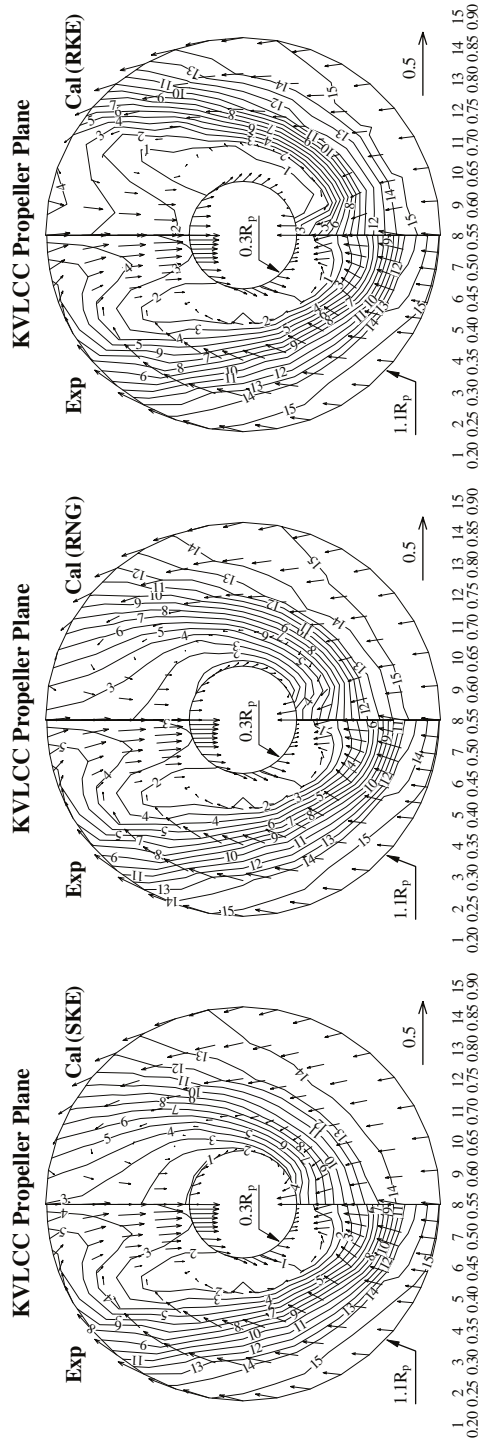
Figure 17. Comparison of velocity fields at propeller plane of KVLCC using three different turbulence models (left: SKE, centre: RNG, right: RKE).
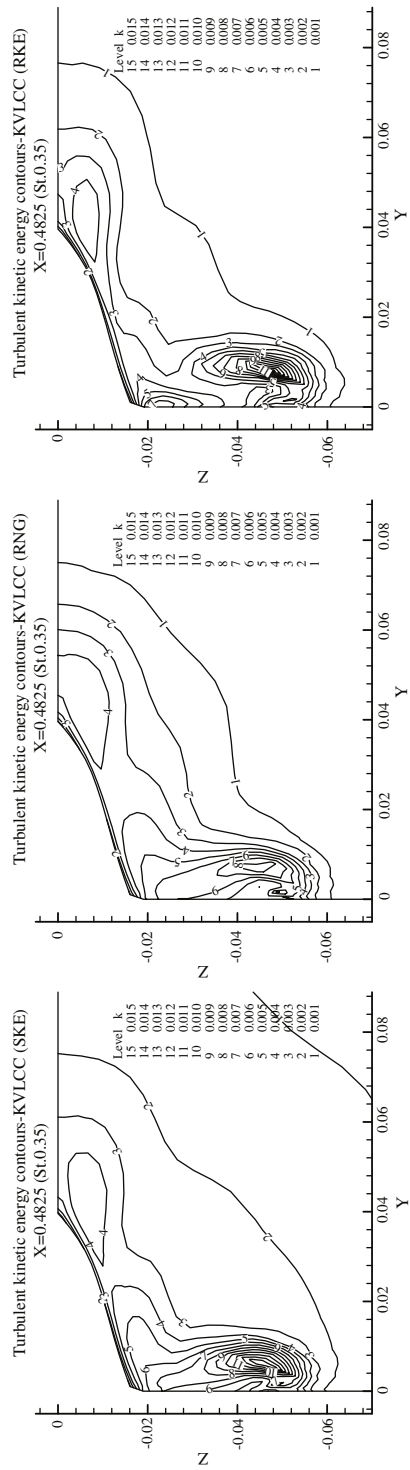
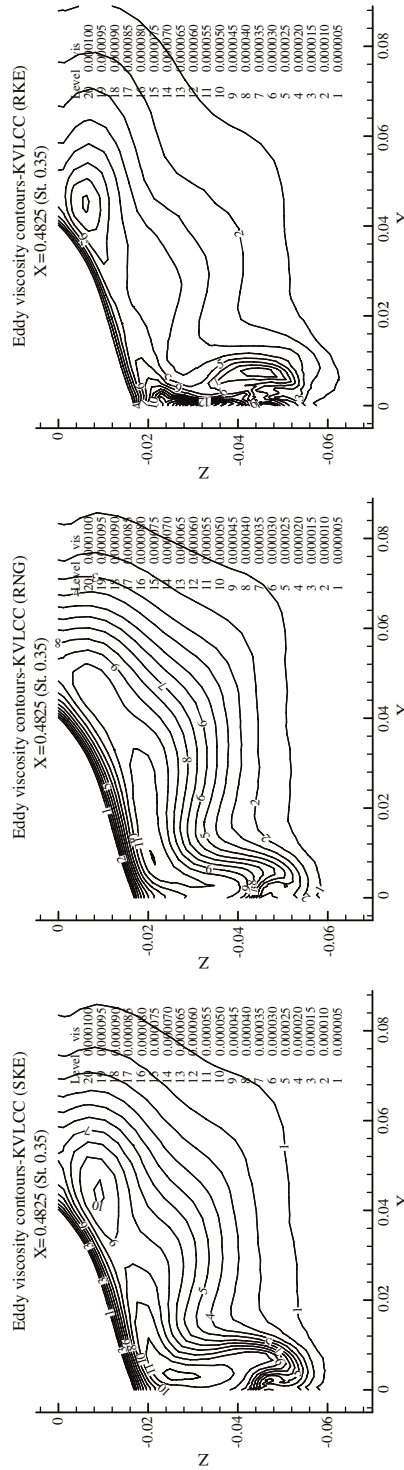Figure 18. Calculated turbulent kinetic energy at $x = 0.4825$ of KVLCC (left: SKE, centre: RNG, right: RKE)

Figure 19. Calculated eddy viscosity at $x = 0.4825$ of KVLCC (left: SKE, centre: RNG, right: RKE).
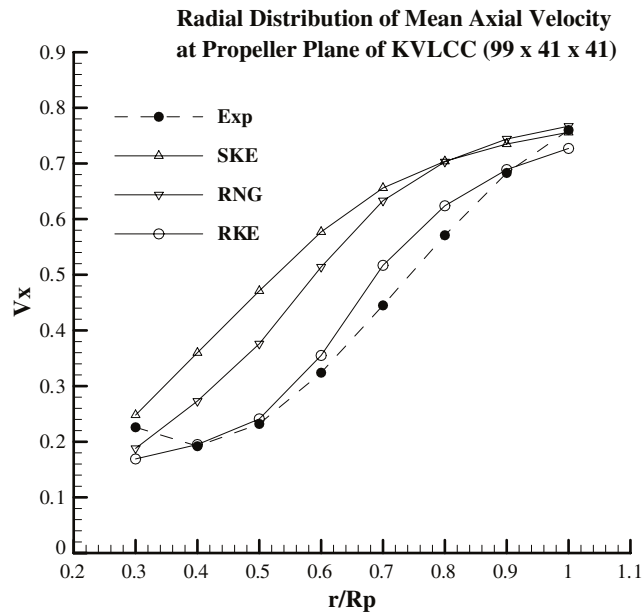
Figure 20. Comparison of radial distribution of circumferentially averaged axial velocity components at propeller plane of KVLCC using three different turbulence models.

4.4. Hull form differences

The propeller plane wakes are investigated carefully for two hull forms with stern frameline modification to see that the present computational modelling can identify the difference of stern hull form quantitatively as well as qualitatively.

As already shown in Figure 7, boundary layer profiles of KVLCC2 show more distortion than those of KVLCC, as expected from stronger turn of bilge shape. The distortion of axial velocity contours is clearly observed near the stern bulb ($z = -0.04$, $y = -0.015$) of both ship models. The strong distortion of axial velocity contour at the propeller plane implies the formation of bilge vortices. The difference of vortex strength is more clearly seen at the propeller plane, as shown in Figure 21(a). Both ships show the hook-like axial velocity contours and the strong transverse vortical flows are seen. As noted earlier, KVLCC2 has more U-shaped stern frame lines, which is also observed in the axial velocity contours. The distortion of velocity contours is more severe in KVLCC2, implying that stronger bilge vortices are formed. The depth of hook is clearer at $U = 0.4$ and 0.35 contours of KVLCC2.

Figure 21(b)–(d) shows the calculated wake distribution for KVLCC and KVLCC2. All three turbulence models make some differences in wakes between two hull forms, although those of SKE and RNG are quite different from the experiment. RKE provides a very reasonable difference between KVLCC and KVLCC2. The radial distributions of circumferentially averaged axial velocity are shown in Figure 22. The shape of axial velocity contours of KVLCC2 in Figure 21 shows a clearer hook shape and becomes closer to a concentric circle. As a result, the wake distribution becomes more uniform in circumferential and radial direction. This distribution is more favourable and preferable for the design of propeller with higher
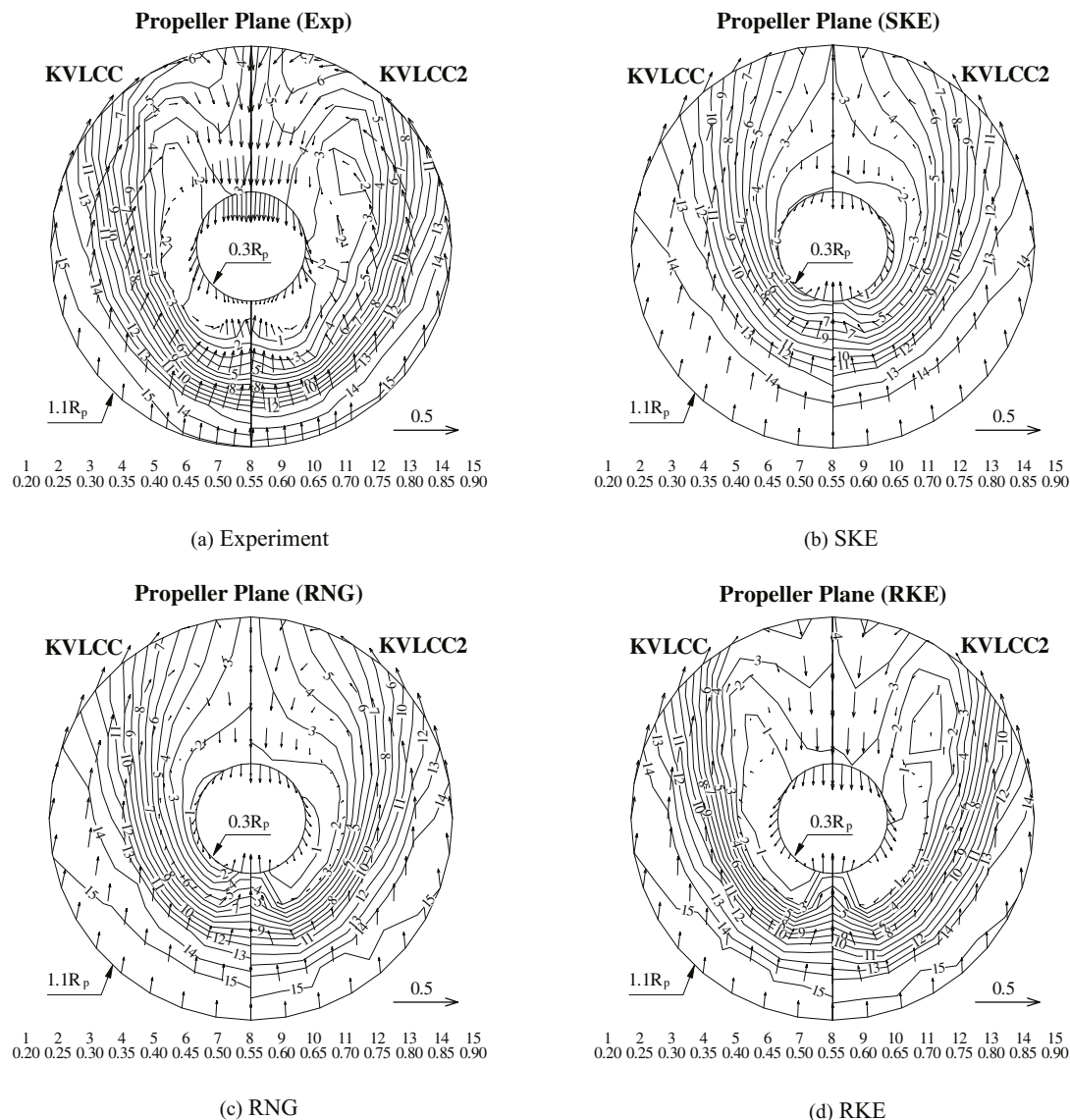
Figure 21. Comparison of propeller plane wake of KVLCC and KVLCC2.

efficiency. The velocity of KVLCC2 near the hub becomes higher than KVLCC, however, outside of 0.55 R_p, the velocity of KVLCC2 becomes smaller. The variation of velocity for KVLCC2 between the hub and tip at the propeller plane is smaller than that of KVLCC. Surprisingly all three models give almost the same amount of difference between the two ships, except near hub. If the viscous calculation was used only for the qualitative purpose, SKE or RNG should have given the right answer, although the values are not in good agreement with the experiment. The other point from the present calculation is that calculated wake
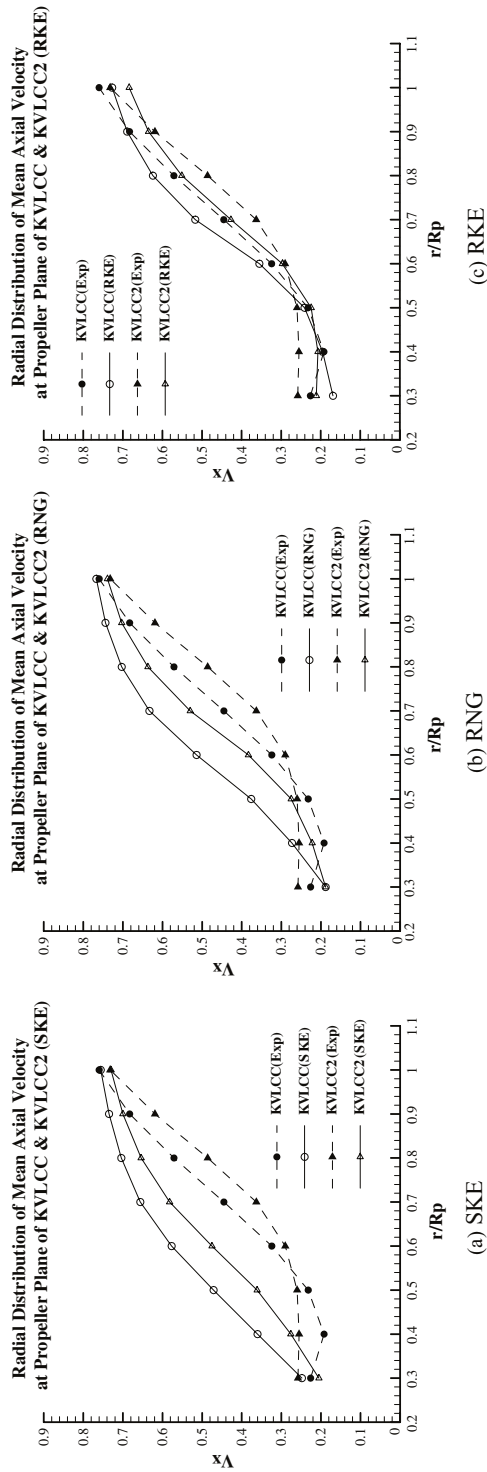
Figure 22. Comparison of radial distribution of axial velocity components at propeller plane wake of KVLCC and KVLCC2 using three turbulence models.
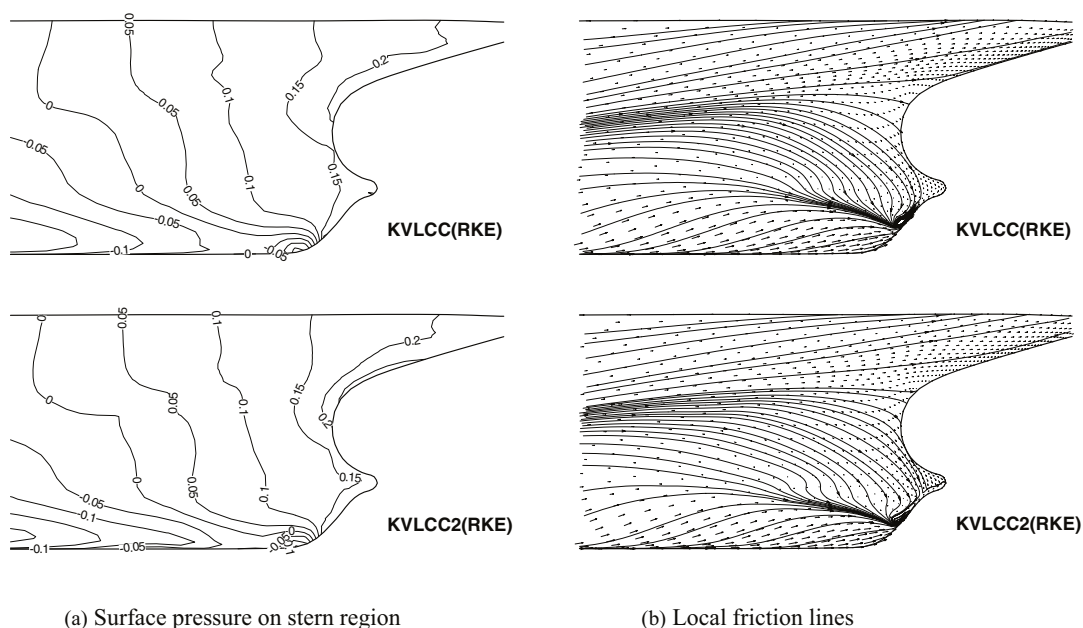
(a) Surface pressure on stern region   (b) Local friction lines

Figure 23. Calculated surface pressure and friction lines on KVLCC and KVLCC2 with RKE.

Table II. Comparison of drag coefficients.

Ship	KVLCC				KVLCC2			
Reynolds number	4.6×10^6 (model scale)				4.6×10^6 (model scale)			
Turbulence model	Exp	SKE	RNG	RKE	Exp	SKE	RNG	RKE
$C_F \times 1000$	3.450	3.728	3.441	3.355	3.450	3.732	3.444	3.359
$C_{VP} \times 1000$	0.638	1.010	0.313	0.475	0.660	1.049	0.351	0.518
Nominal wake	0.523	0.380	0.409	0.500	0.561	0.444	0.481	0.549

distribution with RKE gives fairly good agreement with the experiment. One of the conclusions drawn from the present computation is that it is possible to predict nominal wake distribution in pretty good accuracy with RKE and wall function.

Surface pressure and friction lines on KVLCC and KVLCC2 with RKE are shown in Figure 23. There is little difference in pressure. However, this difference will make some difference in viscous pressure drag, since pressure distribution near the stern region will directly affect the pressure drag. Limiting streamlines of KVLCC2 near the stern region shows a little stronger convergence into open separation line than in KVLCC, but difference is not very notable. However, it should be mentioned here that this amount of frame line change is usually applied in shipyards for hull form optimisation.

Finally, integrated parameters are compared in Table II. The experimental data given in the table is the frictional resistance coefficient and residuary resistance coefficient, based on 1957 ITTC skin friction lines, while the calculated results are integrated frictional and pressure drag

coefficients. Surface friction coefficients of KVLCC and KVLCC2 with the same turbulence model are very similar, while a difference is found between the turbulence models. However, there are bigger differences in viscous pressure drag coefficients and nominal wake. SKE again failed to predict the pressure drag. RKE are the closest, since the wave making the resistance coefficient of the present VLCCs at the Froude number of 0.142 is about 0.15×10^{-3}. In nominal wake prediction, as noted earlier, RKE gives pretty close values to the experimental data.

As noted earlier, the difference in stern hull forms of KVLCC and KVLCC2 is not very large, thus, the global features of the stern flows are similar. However, the changes of velocity distribution at the propeller plane are notable. It is encouraging that the present computational modelling with a relatively simple turbulence model could tell the difference in nominal wakes of two similar hull forms.

5. CONCLUDING REMARKS

A computational study is performed to confirm that the viscous flow calculation with affordable difficulties can predict correctly the nominal wake distribution of a full form tanker. Calculations are carried out for the two modern practical VLCC ship models with the scale ratio of 1/58, having the same forebody and the slightly different afterbodies, i.e., KVLCC and KVLCC2. The focus is laid upon the application of relatively simple computational modelling in routine design process of hull form. An efficient surface mesh and field grid generating method is suggested to enhance the usability of CFD in initial hull form design stage. Surface meshes are generated algebraically starting from an offset table, while the combination of the elliptic and algebraic grid generation methods is used to obtain the 3D field grid system.

The Reynolds-averaged Navier–Stokes equations for turbulent flows around model ships are solved using the cell-centred finite-volume schemes. Several variations of the two-equation turbulence model, such as the standard $k-\varepsilon$ model (SKE), the RNG-based $k-\varepsilon$ model (RNG), and the realisable $k-\varepsilon$ model (RKE), are evaluated to identify the difference caused by the turbulence model. It is observed that the realisable $k-\varepsilon$ model provided realistic wake distribution with a hook-like shape, while the other two turbulence models failed. However, all three turbulence models provided the right differences in nominal wake distribution between two VLCC ship models. It is encouraging to see that the CFD with relatively simple turbulence closure can tell the difference quantitatively as well as qualitatively for the two hull forms with stern frame line modification.

It is premature to state that the present computational modelling is still valid and useful to predict the stern flow around full-scale ships, whose Reynolds numbers are usually over 1.0×10^{9}, since the results only in the model scale are presented. The turbulence model should be validated for such very high Reynolds number flows, although the numerical methods can be considered to be useful. However, measurement of very high Reynolds flow such as the stern flow of a prototype ship is very difficult and costly. Nevertheless, for the hull form designer, the flow information in model scale is still useful to judge the superiority in resistance and propulsive performance among hull forms.

The present computational method with the simple turbulence model (RKE) can predict resistance coefficients and nominal wake fractions with acceptable accuracy compared to the towing tank model experiment. Furthermore, it takes less than 3 h on PC to complete the

grid generation and flow calculation starting from the offset table. It is quite certain that the viscous flow calculation method can be a useful tool in the initial design process of hull forms.

REFERENCES

1. ITTC. *Proc. of the 22nd International Towing Tank Conference*, Seoul, 1999; 188–205.
2. Larsson L, Patel VC, Dyne G (eds). Ship viscous flow. *Proc. of 1990 SSPA-CTH-IIHR Workshop*, Gothenburg, Sweden, 1991.
3. Kodama Y (ed). *Proc. of CFD Workshop Tokyo – An International Workshop for Improvement of Hull Form Designs*, Tokyo, Japan, 1994.
4. Sorenson RL. A computer program to generate two-dimensional grids about airfoils and other shapes by the use of Poisson equation. *NASA TM 81198*, 1980.
5. Van SH, Kim WJ, Kim DH, Lee CJ. Experimental study on the flow characteristics around VLCC with different stern shapes. *Proc. of the Third International Conference on Hydrodynamics*, Seoul, Korea 1998; 265–270.
6. Nowaki H, Bloor MIG, Oleksiewicz B. *Computational Geometry for Ships*. World Scientific Publishing Co., 1995
7. Thompson JF, Warsi ZUA, Mastin CW. *Numerical Grid Generation*. Elsevier Science: Oxford, 1985.
8. Hsu K, Lee SL. A numerical technique for two-dimensional grid generation with grid control at all of the boundaries. *Journal of Computational Physics* 1991; **96**:451–469.
9. Schneider GE, Zedan M. A modified strongly implicit procedure for numerical solution of field problems. *Numerical Heat Transfer* 1981; **4**:1–19.
10. Kim WJ, Van SH, Kim DH, Kim HT, Kim JJ. Computational study on turbulent flow around practical hull forms with efficient grid generator. *Proc. of Osaka Colloquium on Advanced Application of CFD on Hull Form Design*, Osaka, Japan 1998; 317–330.
11. Launder BE, Spalding DB. The numerical computation of turbulent flows. *Computer Methods in Applied Mechanics and Engineering* 1974; **3**:269–289.
12. Yakhot V, Orszag SA, Thangam S, Gatski TB, Speziale CG. Development of turbulence models for shear flows by a double expansion technique. *Physics of Fluids A* 1992; **4**:1510–1520.
13. Shih T-H, Liou WW, Shabir A, Zhu J. A new eddy viscosity model for high Reynolds number turbulent flows — model development and validation. *Computers and Fluids* 1995; **24**:227–238.
14. Kim SE. Evaluation of advanced turbulence models for complex external flow past a full ship hull. *FEDSM97-3163*, the 1997 ASME Fluids Engineering Division Summer Meeting, 1997.
15. Ferziger JH, Peric M. *Computational Methods for Fluid Dynamics*. Springer: New York, 1996.